



Publication Year	2018
Acceptance in OA	2020-10-13T14:22:46Z
Title	Peculiar spin frequency and radio profile evolution of PSR J1119-6127 following magnetar-like X-ray bursts
Authors	Dai, S., Johnston, S., Weltevrede, P., Kerr, M., BURGAY, MARTA, Esposito, P., ISRAEL, Gian Luca, POSSENTI, ANDREA, Rea, N., Sarkissian, J.
Publisher's version (DOI)	10.1093/mnras/sty2063
Handle	http://hdl.handle.net/20.500.12386/27768
Journal	MONTHLY NOTICES OF THE ROYAL ASTRONOMICAL SOCIETY
Volume	480

Peculiar spin frequency and radio profile evolution of PSR J1119–6127 following magnetar-like X-ray bursts

S. Dai,¹★ S. Johnston,¹ P. Weltevrede,² M. Kerr,³ M. Burgay,⁴ P. Esposito,⁵ G. Israel,⁶ A. Possenti,⁴ N. Rea^{5,7,8} and J. Sarkissian⁹

¹CSIRO Astronomy and Space Science, Australia Telescope National Facility, Box 76 Epping NSW 1710, Australia

²Jodrell Bank Centre for Astrophysics, The University of Manchester, Alan Turing Building, Manchester, M13 9PL, UK

³Space Science Division, Naval Research Laboratory, Washington, DC 20375-5352, USA

⁴INAF Osservatorio Astronomico di Cagliari, Via della Scienza 5, I-09047 Selargius, Italy

⁵Anton Pannekoek Institute for Astronomy, University of Amsterdam, Postbus NL-94249, 1090GE Amsterdam, the Netherlands

⁶INAF Osservatorio Astronomico di Roma, via Frascati 33, I-00040 Monteporzio Catone, Roma, Italy

⁷Institute of Space Sciences (ICE, CSIC), Campus UAB, Carrer de Can Magrans s/n, E-08193 Barcelona, Spain

⁸Institut d'Estudis Espacials de Catalunya (IEEC), E-08034 Barcelona, Spain

⁹CSIRO Astronomy and Space Science, Parkes Observatory, PO Box 276, Parkes NSW 2870, Australia

Accepted 2018 July 20. Received 2018 July 8; in original form 2018 May 20

ABSTRACT

We present the spin frequency and profile evolution of the radio pulsar J1119 – 6127 following magnetar-like X-ray bursts from the system in 2016 July. Using data from the Parkes radio telescope, we observe a smooth and fast spin-down process subsequent to the X-ray bursts resulting in a net change in the pulsar rotational frequency of $\Delta\nu \approx -4 \times 10^{-4}$ Hz. During the transition, a net spin-down rate increase of $\Delta\dot{\nu} \approx -1 \times 10^{-10}$ Hz s⁻¹ is observed, followed by a return of $\dot{\nu}$ to its original value. In addition, the radio pulsations disappeared after the X-ray bursts and reappeared about two weeks later with the flux density at 1.4 GHz increased by a factor of 5. The flux density then decreased and undershot the normal flux density followed by a slow recovery back to normal. The pulsar's integrated profile underwent dramatic and short-term changes in total intensity, polarization, and position angle. Despite the complex evolution, we observe correlations between the spin-down rate, pulse profile shape, and radio flux density. Strong single pulses have been detected after the X-ray bursts with their energy distributions evolving with time. The peculiar but smooth spin frequency evolution of PSR J1119–6127 accompanied by systematic pulse profile and flux density changes are most likely to be a result of either reconfiguration of the surface magnetic fields or particle winds triggered by the X-ray bursts. The recovery of spin-down rate and pulse profile to normal provides us the best case to study the connection between high magnetic-field pulsars and magnetars.

Key words: pulsars: general – stars: magnetars – pulsars: individual: PSR J1119-6127.

1 INTRODUCTION

Of the more than 2600 pulsars now known, the so-called magnetars form a small subclass with only 29 members¹ (see e.g. Kaspi & Beloborodov 2017; Esposito, Rea & Israel 2018, for reviews). Typically, these pulsars have long rotation periods and very high spin-down rates, hence high inferred surface magnetic fields above a few 10¹³G. Magnetars are characterized by X-ray outbursts whose luminosity exceeds the spin-down luminosity and are therefore likely

to be powered by the ultra-high magnetic fields. In addition, some magnetars have been detected as transient pulsating radio sources, showing several differences from the normal radio pulsars, including extreme variability in their flux densities, pulse profiles, and spin-down rates (Camilo et al. 2006, 2007a,b, 2008; Levin et al. 2012).

If energetic burst activities of magnetars are powered by their magnetic fields, and given that similar behaviour has been seen in sources with inferred magnetic fields in the range of ordinary radio pulsars (such as SGR 0418+5729 and Swift J1822.3 – 1606, Rea et al. 2010, 2012), it is then conceivable that radio pulsars with high inferred surface dipole magnetic fields (hereafter high-*B* pulsars) could exhibit magnetar-like activity (Kaspi & McLaughlin 2005; Ng & Kaspi 2011). Studies have also been carried out to unify the obser-

* E-mail: shi.dai@csiro.au

¹ See <http://www.physics.mcgill.ca/~pulsar/magnetar/main.html> (Olausen & Kaspi 2014)

Table 1. Spin parameters for PSR J1119–6127 following the initial X-ray burst. Error bars on the last digit are given in parentheses.

Epoch (MJD)	57935.25
Spin frequency (ν)	2.438745737(4) Hz
Spin-frequency derivative ($\dot{\nu}$)	$-2.466288(9) \times 10^{-11} \text{ Hz s}^{-1}$
Spin-frequency second derivative ($\ddot{\nu}$)	$3.80(1) \times 10^{-21} \text{ Hz s}^{-2}$
MJD range	57795 – 58208

vational diversity of magnetars, high- B radio pulsars, and isolated nearby neutron stars via magneto-thermal evolution models (Viganò et al. 2013). Previously, only one high- B , rotation-powered pulsar, PSR J1846–0258, has been observed to transition to a magnetar-like phase (Gavriil et al. 2008). While several short magnetar-like bursts and a sudden spin-up glitch followed by a strong overrecovery were detected (Kuiper & Hermsen 2009; Livingstone, Kaspi & Gavriil 2010; Livingstone et al. 2011), no radio activities have been observed. More observational evidences of high- B radio pulsars in the transitional phase are therefore important for us to understand their connection to magnetars, and to unify these two populations of isolated neutron stars.

PSR J1119–6127 is a high- B , rotation-powered radio pulsar discovered in the Parkes multibeam pulsar survey (Camilo et al. 2000); the pulsar’s basic timing parameters are listed in Table 1. It has been regularly observed at the Parkes radio telescope as a part of a monitoring program of energetic pulsars (Weltevrede et al. 2010; Abdo et al. 2013) and two unusual glitches have been detected in the pulsar described in full by Weltevrede, Johnston & Espinoza (2011) and Antonopoulou et al. (2015). In addition, Weltevrede et al. (2011) also detected extremely rare intermittent pulse components following the glitch. Antonopoulou et al. (2015) measured a braking index of $\simeq 2.7$, indicating that in the $P - \dot{P}$ plane the pulsar appears to be moving towards the magnetar population. They also found marginal evidence for a permanent change in the braking index following a glitch.

Magnetar-like X-ray bursts from PSR J1119–6127 were detected by the *Fermi*/gamma-ray Burst Monitor on 2016 July 27 (Younes, Kouveliotou & Roberts 2016) and by the *Swift*/Burst Alert Telescope on July 28 (Kennea et al. 2016). This made PSR J1119 – 6127 the first rotation-powered radio pulsar to show magnetar-like activities. Following the X-ray bursts, the persistent X-ray flux of PSR J1119–6127 increased by a factor of 160, and the pulsar underwent a large glitch (Archibald et al. 2016). Extensive searches in both *Fermi* and *Swift* data for lower luminosity bursts uncovered 10 additional bursts from the source (Göğüş et al. 2016). Additionally, its pulsed radio emission at ~ 1.4 GHz was quenched following the bursts (Burgay et al. 2016a), and only reappeared some two weeks later (Burgay et al. 2016b). Higher radio frequency observations confirmed the initial disappearance of the radio emission and its prompt reactivation and also showed pulse profile evolution over several months of observation (Majid et al. 2017). Simultaneous observations at X-ray, with *XMM*–Newton and NuSTAR, and at radio frequencies with the Parkes radio telescope, showed that the rotationally powered radio emission shut off multiple times, in coincident with the occurrence of X-ray bursts (Archibald et al. 2017). Three months after the bursts, the pulsar was still brighter in the X-rays by a factor of 22 in comparison with its quiescence and the X-ray images revealed a nebula brighter than in the pre-burst *Chandra* observations (Blumer, Safi-Harb & McLaughlin 2017).

In this paper, we present observations of the spin frequency and radio profile evolution of PSR J1119–6127 after the X-ray outburst using data taken with the Parkes radio telescope. The pecu-

liar spin frequency evolution of PSR J1119–6127 together with its magnetar-like activities, provide us an opportunity to study the relation/transition between high- B pulsars and magnetars and to understand the origin of X-ray bursts and the evolution of magnetic fields. In Section 2, we describe the observations and the data reduction. In Section 3, we present the results on spin frequency evolution, flux density, polarization pulse profiles, and single pulses. Discussions and a summary are given in Sections 4 and 5.

2 OBSERVATIONS AND DATA REDUCTION

PSR J1119–6127 is observed regularly using the Parkes radio telescope under the auspices of program P574, with an approximate observing cadence of four weeks. Data taken prior to 2014 are described in Antonopoulou et al. (2015). In this paper, we use observations taken since 2015,² which were primarily carried out in the band centred at 1369 MHz using the central beam of the 20 cm multibeam receiver. From 2016 February to 2016 October the H-OH receiver centred at 1465 MHz was used.

Triggered by the X-ray bursts on 2016 July 27, PSR J1119–6127 was extensively observed in 2016 July, 2016 August, and 2016 September using the Parkes radio telescope as a part of proposal P626 (PI: M. Burgay). Two observing modes, fold-mode and search-mode, were used for the follow-up observations. For fold-mode, data were folded modulo the pulse period with 1024 phase bins in each of 1024 frequency channels, integrated for 30 s and written to disc. For search-mode, data were recorded with 4-bit-sampling every 256 μs in each of 512 frequency channels. For both modes, full Stokes information was recorded. The observing frequency, bandwidth and integration time are presented in Table 2.

For the fold-mode observations, the data-processing procedure follows that described in Kerr et al. (2018). We removed 5 per cent of the bandpass at each edge to mitigate Radio Frequency Interference (RFI) and aliasing and excised data affected by narrow-band and impulsive radio-frequency interference for each sub-integration. To measure the differential gains between the signal paths of the two voltage probes, once an hour we observe a pulsed noise signal injected into the signal path prior to the first-stage low-noise amplifiers. The noise signal also provides a reference brightness for each observation. To correct for the absolute gain of the system, we use observations of the radio galaxy 3C 218 (Hydra A); using on- and off-source pointings, we can measure the apparent brightness of the noise diode as a function of radio frequency. A dispersion measure of 704.8 $\text{cm}^{-3} \text{ pc}$ (Petroff et al. 2013) and a rotation measure (RM) of 853 rad m^{-2} (Johnston & Weisberg 2006) were used in the data processing. All data reduction used the *PSRCHIVE* (Hotan, van Straten & Manchester 2004) software package.

3 RESULTS

3.1 Spin frequency evolution

There are a number of difficulties in solving for the evolution of the pulsar’s spin parameters after the X-ray bursts. First, the profile underwent changes (see Section 3.3) for which no absolute reference point can be used to determine pulse time of arrivals. Secondly, standard pulsar timing software does not cope well with the strong and rapid evolution of both ν and $\dot{\nu}$ seen here. We have therefore not

²When investigating the spin frequency evolution we included spin frequency measurements back to 2013.

Table 2. Observing log of PSR J1119–6127. The top portion of the table lists the fold-mode observations with the search-mode observations in the bottom portion. Measured spin frequency and flux density are presented for each observation. For search-mode observations, we also list the number of detection of strong single pulses (No. of SP) with S/N > 10. Profile types are as given in Section 3.3.

Date	MJD	Receiver	Frequency (MHz)	Bandwidth (MHz)	Integration (s)	ν (Hz)	Flux (mJy)	Profile shape	
Fold mode									
2016 May 22	57530.23	HOH	1465	512	180	2.44000(2)	0.97(4)	A	
2016 June 19	57558.18	HOH	1465	512	180	2.43991(2)	1.01(4)	A	
2016 July 24	57593.05	HOH	1465	512	180	2.43986(1)	0.97(4)	A	
2016 Aug 9	57609.14	HOH	1369	256	970	2.439801(5)	0.29(1)	A	
2016 Aug 9	57609.19	HOH	1369	256	940	2.439811(6)	0.34(2)	A	
2016 Aug 9	57609.33	HOH	1369	256	600	2.439824(6)	0.56(2)	A	
2016 Aug 11	57611.21	HOH	1369	256	640	2.439803(6)	0.65(2)	A	
2016 Aug 12	57612.03	HOH	1369	256	460	2.439823(9)	1.05(3)	B	
2016 Aug 12	57612.04	HOH	1465	512	330	2.43981(1)	1.08(2)	B	
2016 Aug 13	57613.37	HOH	1369	256	500	2.439803(2)	2.18(3)	B	
2016 Aug 15	57615.07	HOH	1369	256	150	2.43977(2)	2.80(5)	B	
2016 Aug 19	57619.12	HOH	1369	256	300	2.43977(1)	3.77(5)	B	
2016 Aug 19	57619.16	HOH	1465	512	180	2.43979(1)	2.63(4)	B	
2016 Aug 19	57619.18	HOH	1369	256	780	2.439781(3)	3.08(3)	B	
2016 Aug 19	57619.19	HOH	1369	256	550	2.439780(4)	2.64(3)	B	
2016 Aug 19	57619.20	HOH	1369	256	350	2.43980(1)	2.41(4)	B	
2016 Aug 19	57619.97	HOH	1465	512	1200	2.439780(1)	2.69(2)	B	
2016 Aug 24	57624.98	HOH	1369	256	1200	2.439760(1)	3.15(2)	B	
2016 Aug 25	57625.03	HOH	1369	256	610	2.439756(4)	2.68(3)	B	
2016 Aug 26	57626.02	HOH	1369	256	490	2.439748(5)	2.55(3)	B	
2016 Aug 29	57629.88	HOH	1369	256	1200	2.43973(2)	3.31(3)	C	
2016 Aug 29	57629.91	HOH	1369	256	810	2.439724(1)	3.26(3)	C	
2016 Aug 30	57630.09	HOH	1369	256	1200	2.439723(1)	3.48(4)	C	
2016 Aug 30	57630.17	HOH	1369	256	1200	2.439725(1)	3.84(4)	C	
2016 Aug 30	57630.21	HOH	1369	256	1200	2.4397241(8)	4.29(4)	C	
2016 Aug 31	57631.02	HOH	1369	256	1200	2.4397157(8)	4.83(5)	C	
2016 Aug 31	57631.03	HOH	1369	256	1200	2.4397178(8)	5.05(5)	C	
2016 Aug 31	57631.05	HOH	1369	256	1200	2.4397178(8)	4.99(5)	C	
2016 Sep 01	57632.14	HOH	1369	256	520	2.439700(5)	4.35(8)	C	
2016 Sep 01	57632.15	HOH	1369	256	1200	2.4397054(9)	4.77(6)	C	
2016 Sep 01	57632.17	HOH	1369	256	1550	2.439706(1)	4.46(7)	C	
2016 Sep. 04	57635.87	HOH	1369	256	1250	2.439670(1)	3.95(8)	C	
2016 Sep 04	57635.91	HOH	1369	256	400	2.439672(4)	3.83(4)	C	
2016 Sep 25	57656.84	HOH	1369	256	1380	2.439520(4)	0.93(7)	A	
2016 Oct 14	57675.84	HOH	1465	512	1200	2.439371(4)	0.29(1)	A	
2016 Nov 12	57704.75	HOH	1465	512	1200	2.439251(5)	0.14(1)	A	
2016 Dec 10	57732.72	MB	1369	256	1200	2.439186(4)	0.60(2)	A	
2017 Jan 8	57761.60	MB	1369	256	1200	2.43909(1)	0.31(2)	A	
2017 Feb 11	57795.51	MB	1369	256	1200	2.439046(6)	0.83(2)	A	
2017 Mar 19	57831.45	MB	1369	256	1200	2.438958(5)	0.82(2)	A	
2017 Apr 09	57852.37	MB	1369	256	1200	2.438925(4)	0.92(2)	A	
2017 June 05	57909.21	MB	1369	256	300	2.438803(4)	0.93(5)	A	
Search mode									
Date	MJD	Receiver	Frequency (MHz)	Bandwidth (MHz)	Integration (s)	ν (Hz)	No. of SP	Flux (mJy)	Pulse shape
2016 Aug 9	57609.15	HOH	1369	256	2586	2.439816(2)	0	0.21(1)	A
2016 Aug 9	57609.34	HOH	1369	256	3355	2.439818(3)	0	0.21(1)	A
2016 Aug 12	57612.05	HOH	1369	256	287	2.43981(1)	2	1.12(3)	B
2016 Aug 13	57613.38	HOH	1369	256	1303	2.439805(1)	15	2.43(2)	B
2016 Aug 15	57615.08	HOH	1369	256	363	2.439794(5)	17	3.15(3)	B
2016 Aug 29	57629.90	HOH	1369	256	1123	2.4397243(9)	3	3.25(3)	C
2016 Aug 30	57630.19	HOH	1369	256	1433	2.4397234(6)	8	3.07(2)	C
2016 Sep 1	57632.19	HOH	1369	256	1866	2.4397051(2)	45	5.58(2)	C
2016 Sep 4	57635.89	HOH	1369	256	1783	2.4396693(4)	1	3.22(2)	C
2018 Apr 20	58228.61	MB	1369	256	1273	2.450800(3)	0	0.92(2)	A

attempted a phase-coherent fit over this time interval. Rather, we form an analytic template for each observation and then measure ν by fitting pulse time of arrivals of individual sub-integrations across the observation duration.

In the top panel of Fig. 1, we show ν as a function of time with the $\dot{\nu}$ measured by Antonopoulou et al. (2015) shown as the red line and the X-ray outburst shown as the yellow region. Before the X-ray bursts, $\dot{\nu}$ agrees with the previous measurement. However, after the X-ray bursts, ν starts to decrease rapidly as shown in the second panel of Fig. 1 (created after removing the slope due to $\dot{\nu}$). Archibald et al. (2016) reported a large glitch at MJD = 57596.547 ($\Delta\nu = 1.42(2) \times 10^{-5} \text{ s}^{-1}$), but because of the absence of radio emission during that period of time, we cannot confirm the glitch and did not observe significant discrete changes of ν . On the contrary, after the reactivation of radio emission we observed a relatively fast and smooth decrease in ν followed by a rapid drop. This is completely at odds with normal glitches, which have the opposite sign change of ν and happen virtually instantaneously (Palfreyman et al. 2018). Within a time period of ~ 150 days, we observed a net change in the rotational frequency by $\Delta\nu \approx -4 \times 10^{-4} \text{ Hz}$.

The strong evolution of ν is accompanied by rapid changes in $\dot{\nu}$. We fitted for $\dot{\nu}$ using adjacent measurements of ν ; during the rapid changes of ν (MJD between 57600 and 57950), we used a sliding window of 10 days; for the rest of the data set, we used a sliding window of 60 days.³ No significant discrete change of $\dot{\nu}$ was observed after the reactivation of radio emission. The evolution of $\dot{\nu}$ started with a fast and smooth decrease, peaked at MJD ≈ 57632 , and then gradually recovered to its original value. Again, this is different from the recovery of $\dot{\nu}$ following normal glitches and previous glitches observed for this pulsar. What is also interesting is the wiggle during the fast decrease of $\dot{\nu}$ (becoming more negative), and we will discuss this in Section 4.

A large spin-up glitch has been detected for PSR J1846–0258 after the onset of magnetar-like behaviour, followed by an unusually large glitch recovery (Livingstone et al. 2010). While the net spin-down of PSR J1846–0258 after the event ($\Delta\nu \approx -10^{-4}$) is of the same order as we observed for PSR J1119–6127, the evolution of ν is different. We did not see sudden changes in the ν and $\dot{\nu}$ for PSR J1119–6127, and $\dot{\nu}$ peaks about 30 days after the X-ray bursts before recovering back to normal about 200 days later.

An updated timing solution for the pulsar was obtained after the recovery to the normal state (MJD ≈ 57795); these parameters are listed in Table 1.

3.2 Flux density

To measure the flux density, we first formed noise-free standard templates for each observation by fitting scaled von Mises functions (using the `PSRCHIVE` program `PAAS`) to the observed profile after integrating the data over the observing band and observation duration. The `PSRCHIVE` program `PSRFLUX` was used to measure the flux density for each observation, which cross-correlates the observed profile with the standard template to obtain the scaling factor and then the averaged flux density. The uncertainty of flux density was estimated using the standard deviation of the baseline fluctuations. In the bottom panel of Fig. 1, we present the measured flux density as a function of time. After the reactivation of radio emission, the flux density increased rapidly and peaked at MJD ≈ 57632 (black

dashed lines) and then started decreasing. Intriguingly, the flux density undershot the normal flux density ($\sim 1 \text{ mJy}$) and dropped to a minimum value of $\sim 0.14 \text{ mJy}$ and then slowly recovered back to normal. We note that the peak of flux density roughly lines up with the peak of net spin-frequency derivative. Potential correlation between reduced flux density and increased $\dot{\nu}$ has been observed in PSR J1622–4950 (Levin et al. 2012), but it is very different compared with what we have observed for PSR J1119–6127. More similarly, Camilo et al. (2007b) reported a decrease of flux density and a broadening of the pulse profile components accompanied by a decrease in torque of about 10 per cent over an interval of two weeks for XTE J1810–197.

3.3 Profile variations

The polarization characteristics of the pulsar were described in Johnston & Weisberg (2006) and in more detail by Rookyard et al. (2017). In brief, in what we will refer to as the normal state (Profile A), the pulsar shows a single, highly linearly polarized component with a half width of 19° (Johnston & Kerr 2018) and a small amount of circular polarization. The position angle (PA) has a shallow negative slope as a function of phase. In the single abnormal observation directly after a large glitch described by Weltevrede et al. (2011), an extra component, also highly linearly polarized, appeared to lead the normal component. Rookyard et al. (2017) considered both these profiles and concluded the angle between the magnetic and rotation axes, α , was relatively small.

In the observations under consideration here, dramatic changes in the pulse profile and the polarization characteristics were observed between 2016 August 12 and 2016 September 4. Broadly speaking, two alternative profiles are observed. The first, present between 2016 August 12 and 2016 August 26 shows the presence of two components (see Fig. 2) which we call Profile B. The first component is highly polarized whereas the second is not. The circular polarization underwent strong transformation within this period as did the PA swing. In particular, the slope of the PA swing changed from negative to positive during this timeframe. The second state occurred between 2016 August 29 and (at least) 2016 September 4. In this state, Profile C, there are four components (see Fig. 3), a leading small highly polarized component separated in phase from a triple structure with a highly polarized first component followed by two, less polarized components. The relative amplitude of the components changes with time. The circular polarization and the PA swing are again highly variable. As shown above, the pulsar was much brighter during this period, largely due to the third component of the triple structure. There are no observations between 2016 September 4 and 2016 September 25 where the pulsar flux density dropped from $\sim 4 \text{ mJy}$ to $\sim 1 \text{ mJy}$, but the pulse profile appears to have returned to its normal profile on 2016 September 25.

Several questions arise: how do the profiles align in phase, how do the profiles change correlate with the changes in ν and $\dot{\nu}$, and what are the causes of the profile changes?

Considering first the profile alignment, we believe the most plausible solution is that shown in Figs 2 and 3, with zero phase defined as the peak of the profile A, the leading component of the profile B and the leading component of profile C as shown. The implication of this is that the normal component remains roughly constant in amplitude through the other changes, and that the trailing, very bright component seen at later times appears to emerge rapidly between August 26 and 29. In addition, this would imply that the extra component seen in Weltevrede et al. (2011) is aligned in phase with the trailing bright component seen at later times here. What is most

³We treated ν measurements before and after the X-ray bursts separately, and therefore $\dot{\nu}$ before and after the X-ray bursts are independent.

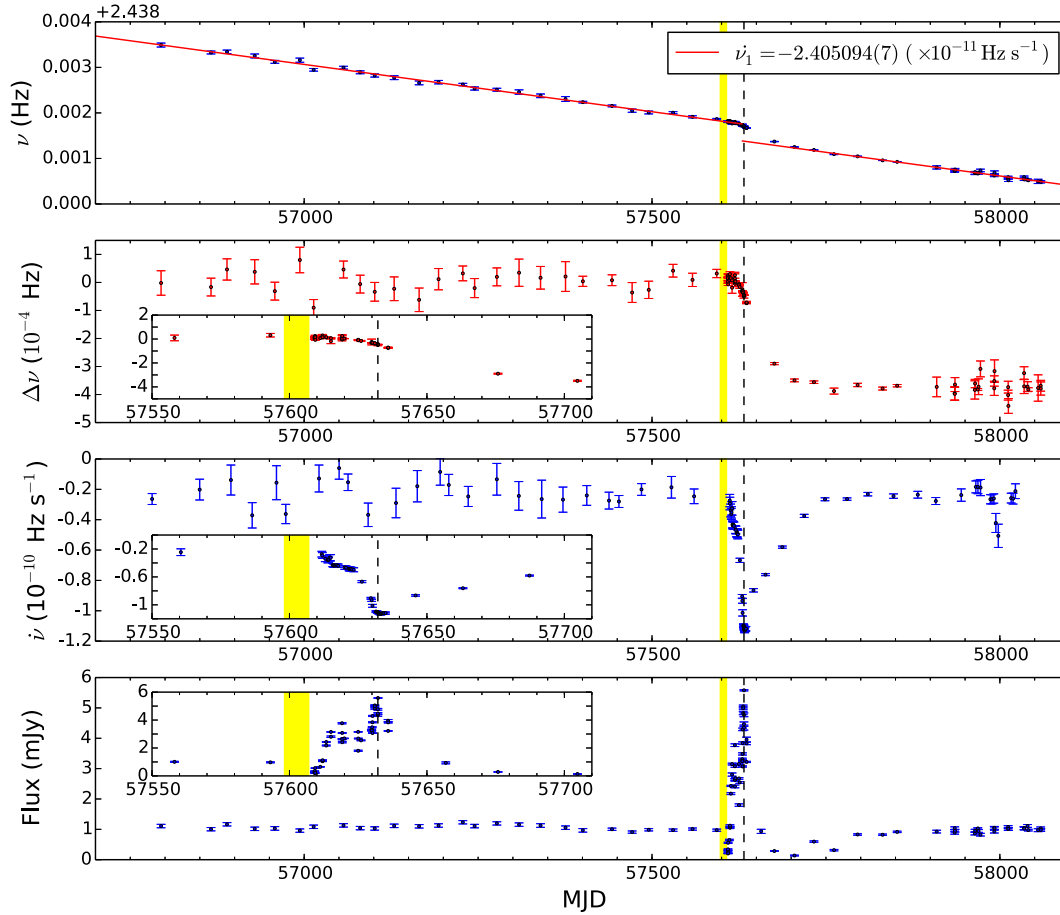


Figure 1. Pulsar spin frequency (ν), spin-frequency derivative ($\dot{\nu}$), and flux density as a function of time. The yellow regions show the radio-quiet period after the X-ray burst. The black dashed lines indicate the peak of flux density.

unexpected about these observations is the extreme changes seen in the PA swing as a function of epoch. No evidence of changes in PA swing has been observed before (Weltevrede et al. 2011). For many pulsars, and for this pulsar in particular, the swing of PA is used to determine the geometry of the star via the rotating vector model (RVM) (Rookyard et al. 2017). The sign of the slope of the PA swing is used to determine whether the line of sight cuts poleward or equatorward from the magnetic axis (Everett & Weisberg 2001), and therefore should not change. The PA swing of these observations significantly deviates from RVM-like behaviour, and for the scope of this paper we have not attempted to model the swing of PA. We also note that no significant changes of RM have been observed following the X-ray bursts.

3.4 Single pulses

Bright individual pulses have been observed for J1119–6127 previously. Weltevrede et al. (2011) detected four strong single pulses at 1.4 GHz on 2007 August 20 and a number of bright single pulses at 3.1 GHz on 2007 July 23. The fact that the strong pulses do not align with the peak of the averaged pulse profile suggests their RRAT-like (Rotating radio transient) origins. Intriguingly, a large amplitude glitch occurred directly before these very rare RRAT-like events were observed. This was the first time that a glitch, or the post-glitch recovery process, has been observed to influence the radio emission process of a normal (non-RRAT) pulsar. A star-

quake model with crustal plate movement has been proposed to explain the changing emission properties coincident with the glitch (Akbal et al. 2015), as well as the unusual glitch recovery (see Antonopoulou et al. 2015).

After the X-ray bursts of J1119 – 6127, we also detected strong single pulses. Out of 10 search-mode observations, we detected strong single pulses with signal-to-noise (S/N) larger than 10 in seven observations. In Table 2, we list the number of detections of strong single pulses with S/N > 10 for each observation. To better understand the occurrence of single pulses, we produced pulse-component-averaged flux density distributions of these observations. The `PSRSALSA` software package (Weltevrede 2016) was used to carry out manual RFI mitigation, to calculate pulse energies, and to fit energy distributions. In the top panel of each subplot in Fig. 4, we show pulse-component-averaged flux density distributions of observations taken on 2016 August 9, 2016 August 13, and 2016 August 30 and on 2016 September 1 and 2016 September 4, all of which show strong single pulses and have integration time long enough for us to study their statistics. In comparison, results of an observation taken during the pulsar’s normal state (2018 April 20) are also shown. Flux density distributions of the main pulse component (centred at a pulse longitude of zero degrees in Figs 2 and 3) and the bright trailing component (centred at a pulse longitude of ~ 25 degrees in Fig. 3) are shown as blue and red histogram, respectively. The standard deviation of the noise distribution is shown as a point with horizontal error bar for each pulse component. The

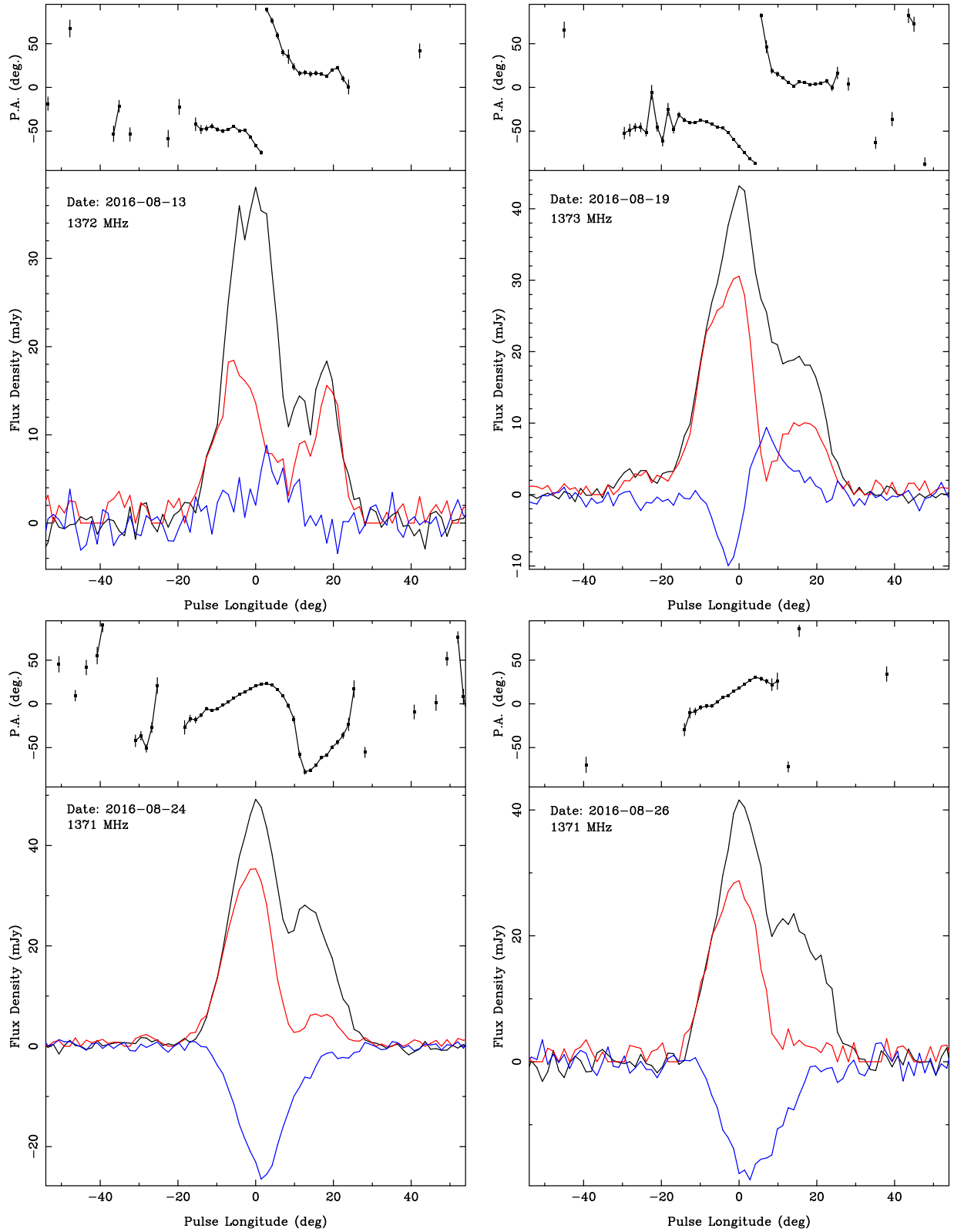


Figure 2. Four examples of Profile B, the two-component profile of PSR J1119–6127. In each panel, the black line shows total intensity, red linear polarization, and blue circular polarization. The PA of the linear polarization, referred to infinite frequency, is also shown. Phase zero has been set according to the discussion in the text.

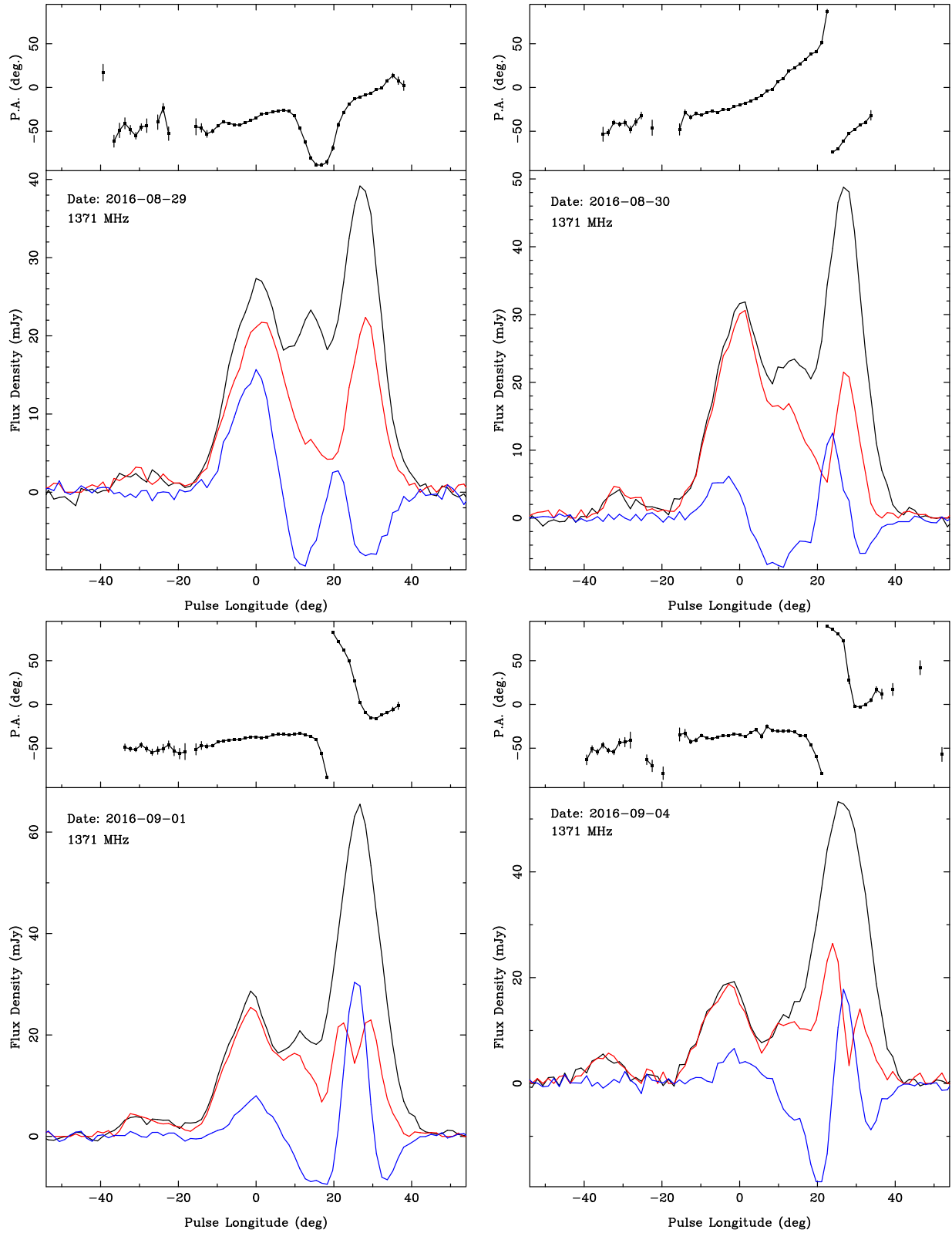


Figure 3. Four examples of Profile C, the four-component profile of PSR J1119–6127. In each panel, the black line shows total intensity, red linear polarization, and blue circular polarization. The PA of the linear polarization, referred to infinite frequency, is also shown. Phase zero has been set according to the discussion in the text.

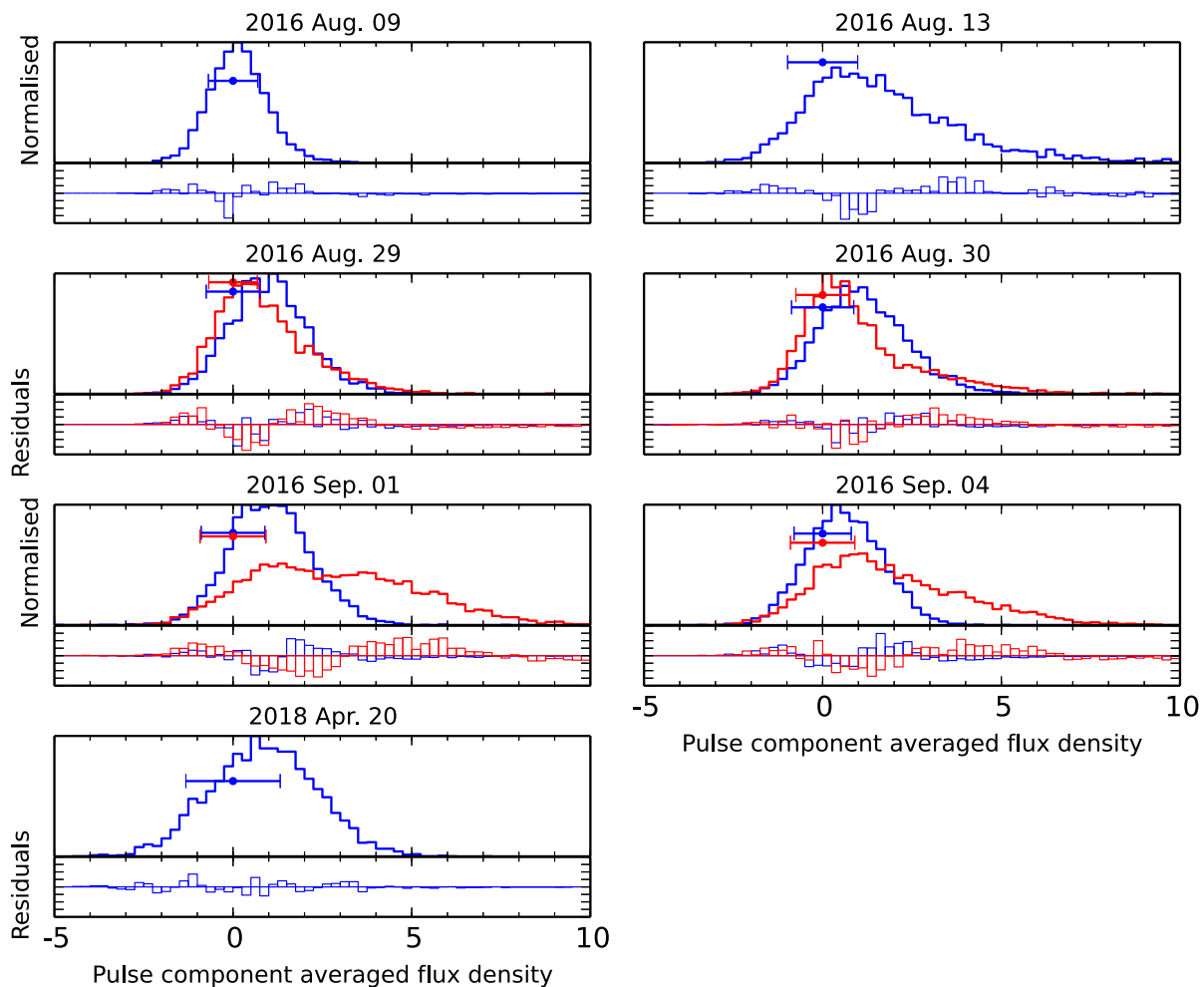


Figure 4. Top panel of each subplot: averaged flux density distributions of individual pulse components (Blue: the main pulse component centred at a pulse longitude of zero degrees in Figs 2 and 3; Red: the trailing component centred at a pulse longitude of ~ 25 degrees in Fig. 3). The standard deviation of the noise distribution is shown as a point with horizontal error bar for each pulse component. Bottom panel of each subplot: fitting residuals of the flux density distribution against a log-normal distribution convolved with the observed noise distribution.

observed energy distribution of single pulses is the intrinsic distribution convolved with the noise, and we fitted for the intrinsic energy distribution as described in Weltevrede (2016), assuming a log-normal distribution. In the bottom panel of each subplot in Fig. 4, we show the fitting residuals for each pulse component.

The energy distribution of both the main and the trailing component significantly deviate from a log-normal distribution after the X-ray bursts. For the trailing component, we observed a long high-energy tail, and it became more and more significant as the pulsar became brighter and showed a new high-energy component on 2016 September 1 before it faded away. For the main component, the energy distributions of observations with Profile C look similar and can be generally fitted by a log-normal distribution, but are clearly different from that of Profile B on 2016 August 13 which deviates from a log-normal distribution. In comparison, for the normal state (e.g. 2018 April 20), the intrinsic energy distribution of single pulses can be well described by a log-normal distribution. Although detailed modelling of the energy distributions is beyond the scope of this paper, our results show that a significantly greater number of energetic pulses were produced after the X-ray bursts and this can not be simply explained by the increase of the averaged flux density. The different pulse energy distributions of two pulse profile

components at different epochs provide evidences of changes in the pulsar magnetosphere triggered by the X-ray bursts.

In order to study the variation of intensity from pulse to pulse as a function of pulse longitude, we calculated the modulation index defined as equation (1) of Weltevrede et al. (2011) in the spectral domain. In Fig. 5, modulation indices at different pulse phases are shown as blue points with error bars on top of the averaged pulse profiles. The variation of modulation index with pulse longitude shows similar shape for all observations and supports our pulse profile alignment. Averaging over the on-pulse phases, we obtained modulation indices after the X-ray bursts (shown in the upper left corner of each panel of Fig. 5) significantly higher than those observed for most pulsars (Weltevrede, Edwards & Stappers 2006).

4 DISCUSSION

We observe a striking correlation between the profile changes, the flux density variability, and the changes in the timing, particularly the value of $\dot{\nu}$. In Fig. 6, we show the evolution of $\dot{\nu}$ and flux density as a function of time directly following the X-ray bursts within 65 days. Different pulse profile types are indicated with shaded regions. During the rapid evolution of spin frequency (within the

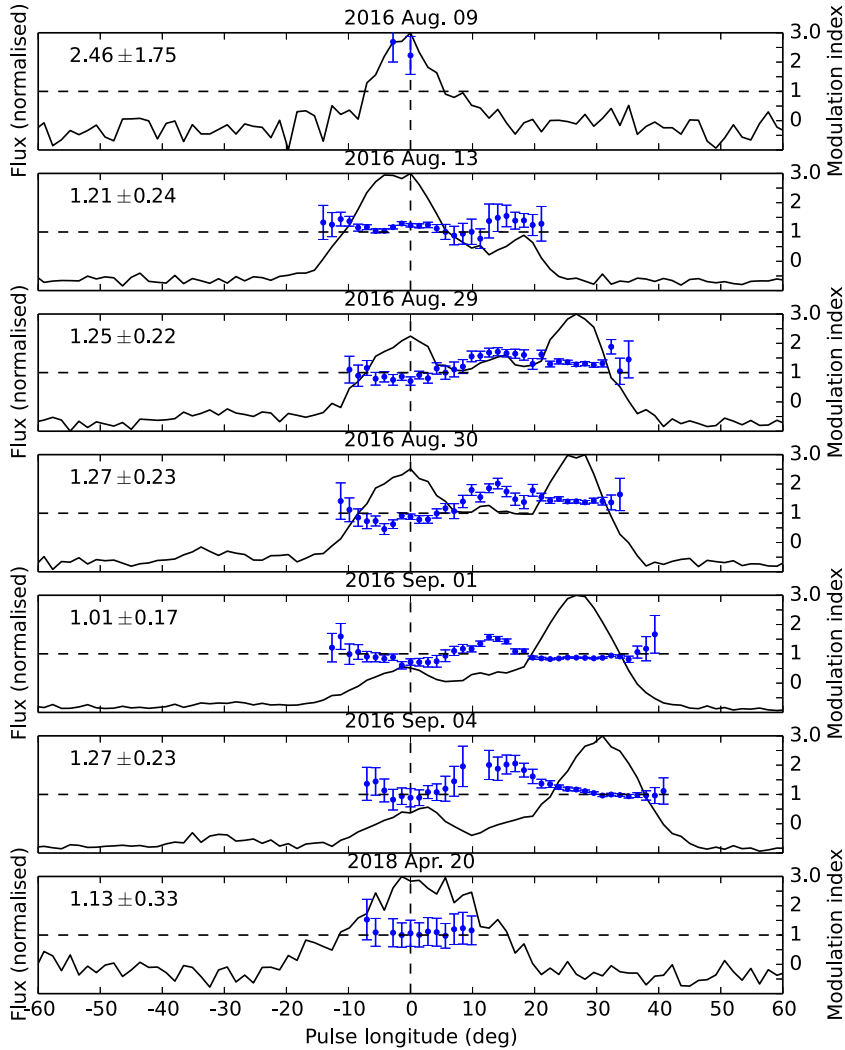


Figure 5. Modulation index (blue points with error bars) as a function of pulse longitude. The averaged pulse profiles are shown as black lines. Averaged modulation indices are presented in the upper left corner of each panel.

first 30 days), the pulse profile changed twice, on 2016 August 12 (MJD ≈ 57612) and 2016 August 29 (MJD ≈ 57630), and at both times we observed fast increase of flux density and decrease of $\dot{\nu}$ (becomes more negative). We also see that for Profile B and Profile C the $\dot{\nu}$ is significantly different by $\sim 0.6 \times 10^{-10} \text{ Hz s}^{-1}$. However, the pulsar has then reverted to its normal profile (MJD ≈ 57656) prior to the slow recovery of $\dot{\nu}$ to its original value.

It therefore seems likely that the torque acting on the pulsar causing the change in ν is also related to the changing pulse profile. This is seen in other pulsars, more specifically in the mode changing pulsars. Lyne et al. (2010) noticed that pulse profile changes were correlated with $\dot{\nu}$ changes. In the pulsars they examined, these changes occurred quickly but then persisted for a time-scale of months (see also Keith, Shannon & Johnston 2013; Brook et al. 2016). In the intermittent pulsar B1931+24 (Kramer et al. 2006) the $\dot{\nu}$ changes appear to be caused by plasma loading in the pulsar magnetosphere. We surmise that something similar is happening in this case.

The only other example of a high- B pulsar transitioning to a magnetar observed so far is the 2006 magnetar-like outburst of PSR J1846–0258 (Gavriil et al. 2008). A large but typical glitch

recovery has been detected for J1846–0258 after the glitch triggered by the X-ray bursts (Livingstone et al. 2010). However, after the reactivation of radio radiation of PSR J1119–6127, we did not observe significant discrete changes of ν and $\dot{\nu}$. On the contrary, a smooth and fast spin-down process with a net spin-down rate change of $\sim 10^{-10} \text{ Hz s}^{-1}$ has been observed, which is much larger than that of PSR J1846–0258 ($\sim 8 \times 10^{-12} \text{ Hz s}^{-1}$) and is clearly different from normal glitch recoveries. Coti Zelati et al. (2018) present the results of a systematic study of all magnetar X-ray outbursts observed to date and show that the total outburst energy of J1119–6127 ($8.5 \times 10^{41} \text{ erg}$) is larger than that of J1846–0258 ($4.5 \times 10^{41} \text{ erg}$). On the other hand, as discussed by Archibald et al. (2016), the X-ray spectra of J1119–6127 in quiescence and during the outburst show different spectral shape and evolution compared with that of J1846–0258. The differences between the behaviour of J1119–6127 and J1846–0258 suggest that the peculiar spin frequency evolution of J1119–6127 reveal processes not well understood during the transition from a high- B radio pulsar to a magnetar.

The net spin-down we observed following the X-ray bursts implies a release of a large amount of rotational energy. Assuming the canonical neutron star moment of inertia of $I_{45} = 10^{45} \text{ g cm}^2$, the

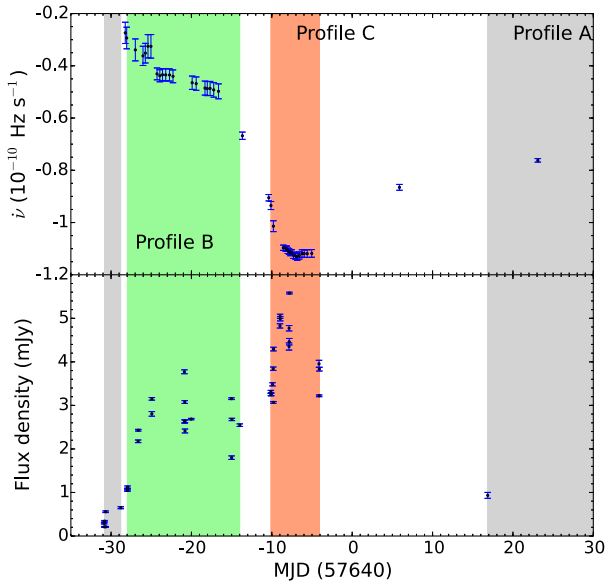


Figure 6. Top: $\dot{\nu}$ as a function of time; Bottom: flux density as a function of time. The grey, green, and red shaded regions represent pulse profiles in type A, B, and C, respectively. We fitted for $\dot{\nu}$ using adjacent measurements of ν with a sliding window as described in Section 3.1, and therefore there are $\dot{\nu}$ points in between different pulse profile types.

rotational energy released can be estimated as

$$\Delta E_{\text{rot}} = 4\pi^2 \nu |\Delta \nu| = 3.8 \times 10^{43} I_{45} \left(\frac{|\Delta \nu|}{4 \times 10^{-4}} \right) \text{ erg.} \quad (1)$$

This is ~ 20 times of the total X-ray outburst energy, and in fact we did not observe obvious correlation between the X-ray light curve presented in Coti Zelati et al. (2018) and the radio flux densities nor the spin-frequency evolution. For a time span of ~ 100 days, the spin-down power gives us an averaged luminosity of $\sim 4.4 \times 10^{36} \text{ erg s}^{-1}$, about two times larger than the normal spin-down luminosity. While only a small portion of the spin-down energy goes into radio and X-ray, we could expect much stronger high energy emissions from the pulsar (e.g. γ -ray) if energy loss via high energy radiation is the main energy-loss mechanism. Such a high spin-down luminosity could also power strong relativistic particle outflows that can brighten the pulsar wind nebula (Blumer et al. 2017).

A complete picture of the PSR J1119–6127 event is likely to be that ultra-strong magnetic fields powered the X-ray bursts and triggered an additional torque that produced the peculiar spin frequency evolution. The fact that the polarization PA changed significantly following the X-ray bursts indicates that the magnetic field might have changed. If we assume that the spin-down process is dominated by dipole braking, the surface magnetic field strength can be estimated as

$$B_s \approx 10^{12} \text{ G} \left(\frac{\dot{P}}{10^{-15}} \right)^{1/2} \left(\frac{P}{\text{s}} \right)^{1/2}, \quad (2)$$

where P and \dot{P} are the spin period and spin-period derivative. Applying equation (2) on our measurements of P and \dot{P} of PSR J1119–6127, we found that after the X-ray burst the surface magnetic field strength can reach as high as $\sim 9 \times 10^{13} \text{ G}$, which is more than two times stronger than the normal field strength. Under such assumptions, the fast increase and slow recovery of $\dot{\nu}$ as shown in

the third panel of Fig. 1 indicate similar evolution of the surface magnetic field strength of the pulsar. This suggests that the X-ray bursts triggered some reconfiguration of the magnetosphere of the pulsar, resulting in the increase of the apparent field strength. The energy of the global dipolar field external to the neutron star can be estimated as

$$E_{\text{dipole}} = \frac{10^{42}}{3} \left(\frac{B_s}{10^{12} \text{ G}} \right)^2 \left(\frac{R}{10 \text{ km}} \right)^3 \text{ erg}, \quad (3)$$

and in order to increase the magnetic field strength from $\sim 4 \times 10^{13} \text{ G}$ to $\sim 9 \times 10^{13} \text{ G}$ a total amount of energy of $\sim 2 \times 10^{45} \text{ erg}$ is needed. This is more than one order of magnitude larger than the spin-down power released following the X-ray bursts. Energies either from multipole (and/or internal) magnetic fields or neutron star interior need to be converted to the strong dipolar field and/or distort the magnetic field. Under such a scenario, the slow recoveries of the timing behaviour and the pulse profile back to normal have to be explained, which might involve the dissipation of the magnetic field.

As an alternative solution, wind braking models have been suggested to explain the spin-down of magnetars (Harding, Contopoulos & Kazanas 1999; Tong et al. 2013) and the antiglitch of magnetar 1E 2259+586 (Tong 2014). Particle winds triggered by the X-ray burst (Thompson & Duncan 1996) can amplify the rotational energy loss rate by providing additional torque to slow down the pulsar. Enhanced particle winds could also be responsible for the fast increase of radio flux density and dramatic changes of pulse profile. Generalizing the model Kramer et al. (2006) proposed to understand different spin-down rates when the intermittent pulsar B1931+24 is on and off, we can estimate the change in charge density in the open field line region as

$$\frac{\Delta \rho}{\rho_{\text{GJ}}} = -2.0 \times \left(\frac{R}{10^4 \text{ m}} \right)^{-6} \left(\frac{B_s}{10^8 \text{ T}} \right)^{-2} \left(\frac{\nu}{1 \text{ Hz}} \right)^{-3} \left(\frac{\Delta \dot{\nu}}{10^{-15} \text{ Hz s}^{-1}} \right), \quad (4)$$

where R is the radius of a neutron star and ρ_{GJ} is the Goldreich-Julian density (Goldreich & Julian 1969). At the maximum net spin-down rate ($\Delta \dot{\nu} \approx 10^{-10} \text{ Hz s}^{-1}$), equation (4) gives us a net change in charge density of $\Delta \rho / \rho_{\text{GJ}} \approx 8.4$, which means that the change in charge density in the open field line region needs to be much larger than ρ_{GJ} . Compared with XTE J1810–197, whose decrease of spin-down rate and flux density and changes of pulse profile have been argued to be caused by a net change of plasma density of $\Delta \rho / \rho_{\text{GJ}} \approx 0.2$ (Camilo et al. 2007b), the extra plasma we need to explain the torque of PSR J1119–6127 is much larger. It is not clear if such high magnetospheric charge densities can be sustained long enough to explain the spin-down of J1119–6127. More realistic pulsar wind and particle acceleration models need to be taken into consideration in order to obtain self-consistent explanations (Li et al. 2014; Xu & Qiao 2001).

5 SUMMARY

We presented the spin frequency, flux density, and pulse profile evolution of PSR J1119–6127 following the X-ray bursts detected in 2016 July, using data taken with the Parkes radio telescope. While PSR J1119–6127 showed radio properties, such as dramatic changes of pulse profile and flux density variability, shared by other magnetars, the peculiar spin frequency evolution is clearly different from what has been observed from magnetars and high- B pulsars

before. Therefore, as the first rotation-powered, radio pulsar to show magnetar-like activities, PSR J1119–6127 provides us the best case to study the connection between high-B pulsars and magnetars.

ACKNOWLEDGEMENTS

The Parkes radio telescope is part of the Australia Telescope National Facility which is funded by the Commonwealth of Australia for operation as a National Facility managed by CSIRO. Work at NRL is supported by NASA. P.E. and N.R. acknowledge funding in the framework of the NWO Vidi award A.2320.0076.

REFERENCES

- Abdo A. A., Ajello M., Allafort A. et al., 2013, *ApJS*, 208, 17
- Akbal O., Güğercinoğlu E., Şaşmaz Muş S., Alpar M. A., 2015, *MNRAS*, 449, 933
- Antonopoulou D., Weltevrede P., Espinoza C. M., Watts A.L., Johnston S., Shannon R.M., Kerr M., 2015, *MNRAS*, 447, 3924
- Archibald R. F., Kaspi V. M., Tendulkar S. P., Scholz P., 2016, *ApJ*, 829, L21
- Archibald R. F., et al., 2017, *ApJ*, 849, L20
- Blumer H., Safi-Harb S., McLaughlin M. A., 2017, *ApJ*, 850, L18
- Brook P. R., Karastergiou A., Johnston S., Kerr M., Shannon R.M., Roberts S.J., 2016, *MNRAS*, 456, 1374
- Burgay M., Possenti A., Kerr M., Esposito P., Rea N., Zelati F.C., Israel G.L., Johnston S., 2016a, *The Astronomer’s Telegram*, 9286
- Burgay M., Possenti A., Kerr M., Esposito P., Rea N., Zelati F.C., Israel G.L., Johnston S., 2016b, *The Astronomer’s Telegram*, 9366
- Camilo F., Kaspi V. M., Lyne A. G., Manchester R.N., Bell J.F., D’Amico N., McKay N.P.F., Crawford F., 2000, *ApJ*, 541, 367
- Camilo F., Ransom S. M., Halpern J. P., Reynolds J., Helfand D.J., Zimmerman N., Sarkissian J., 2006, *Nature*, 442, 892
- Camilo F., Reynolds J., Johnston S., Halpern J.P., Ransom S.M., van Straten W., 2007a, *ApJ*, 659, L37
- Camilo F., et al., 2007b, *ApJ*, 663, 497
- Camilo F., Reynolds J., Johnston S., Halpern J. P., Ransom S. M., 2008, *ApJ*, 679, 681
- Coti Zelati F., Rea N., Pons J. A., Campana S., Esposito P., 2018, *MNRAS*, 474, 961
- Esposito P., Rea N., Israel G. L., 2018, preprint ([arXiv:1803.05716](https://arxiv.org/abs/1803.05716))
- Everett J. E., Weisberg J. M., 2001, *ApJ*, 553, 341
- Gavriil F. P., Gonzalez M. E., Gotthelf E. V., Kaspi V.M., Livingstone M.A., Woods P.M., 2008, *Science*, 319, 1802
- Goldreich P., Julian W. H., 1969, *ApJ*, 157, 869
- Göğüş E., et al., 2016, *ApJ*, 829, L25
- Harding A. K., Contopoulos I., Kazanas D., 1999, *ApJ*, 525, L125
- Hotan A. W., van Straten W., Manchester R. N., 2004, *Publ. Astron. Soc. Aust.*, 21, 302
- Johnston S., Kerr M., 2018, *MNRAS*, 474, 4629
- Johnston S., Weisberg J. M., 2006, *MNRAS*, 368, 1856
- Kaspi V. M., Beloborodov A. M., 2017, *ARA&A*, 55, 261
- Kaspi V. M., McLaughlin M. A., 2005, *ApJ*, 618, L41
- Keith M. J., Shannon R. M., Johnston S., 2013, *MNRAS*, 432, 3080
- Kennea J. A., Lien A. Y., Marshall F. E., Palmer D.M., Roegiers T.G.R., Sbarufatti B., 2016, *The Astronomer’s Telegram*, 9274
- Kerr M., Coles W. A., Ward C. A., Johnston S., Tuntsov A.V., Shannon R.M., 2018, *MNRAS*, 474, 4637
- Kramer M., Lyne A. G., O’Brien J. T., Jordan C. A., Lorimer D. R., 2006, *Science*, 312, 549
- Kuiper L., Hermsen W., 2009, *A&A*, 501, 1031
- Levin L., et al., 2012, *MNRAS*, 422, 2489
- Li L., Tong H., Yan W. M., Yuan J.P., Xu R.X., Wang N., 2014, *ApJ*, 788, 16
- Livingstone M. A., Kaspi V. M., Gavriil F. P., 2010, *ApJ*, 710, 1710
- Livingstone M. A., Ng C.-Y., Kaspi V. M., Gavriil F. P., Gotthelf E. V., 2011, *ApJ*, 730, 66
- Lyne A., Hobbs G., Kramer M., Stairs I., Stappers B., 2010, *Science*, 329, 408
- Majid W. A., Pearlman A. B., Dobrova T., Horiuchi S., Kocz J., Lippuner J., Prince T.A., 2017, *ApJ*, 834, L2
- Ng C.-Y., Kaspi V. M., 2011, *American Institute of Physics Conference Series*, 1379, 60
- Olausen S. A., Kaspi V. M., 2014, *ApJS*, 212, 6
- Palfreyman J., Dickey J. M., Hotan A., Ellingsen S., van Straten W., 2018, *Nature*, 556, 219
- Petroff E., Keith M. J., Johnston S., van Straten W., Shannon R. M., 2013, *MNRAS*, 435, 1610
- Rea N. et al., 2010, *Science*, 330, 944
- Rea N. et al., 2012, *ApJ*, 754, 27
- Rookyard S. C., Weltevrede P., Johnston S., Kerr M., 2017, *MNRAS*, 464, 2018
- Thompson C., Duncan R. C., 1996, *ApJ*, 473, 322
- Tong H., 2014, *ApJ*, 784, 86
- Tong H., Xu R. X., Song L. M., Qiao G. J., 2013, *ApJ*, 768, 144
- Viganò D., Rea N., Pons J. A., Perna R., Aguilera D. N., Miralles J. A., 2013, *MNRAS*, 434, 123
- Weltevrede P., 2016, *A&A*, 590, A109
- Weltevrede P., Edwards R. T., Stappers B. W., 2006, *A&A*, 445, 243
- Weltevrede P., Johnston S., Manchester R. N. et al., 2010, *PASA*, 27, 64
- Weltevrede P., Johnston S., Espinoza C. M., 2011, *MNRAS*, 411, 1917
- Xu R. X., Qiao G. J., 2001, *ApJ*, 561, L85
- Younes G., Kouveliotou C., Roberts O., 2016, *GCN*, 19736

This paper has been typeset from a $\text{\TeX}/\text{\LaTeX}$ file prepared by the author.